



HAL
open science

Sea Surface Temperature in Global Analyses: Gains from the Copernicus Imaging Microwave Radiometer

Kevin Pearson, Simon Good, Christopher Merchant, Catherine Prigent, Owen Embury, Craig Donlon

► **To cite this version:**

Kevin Pearson, Simon Good, Christopher Merchant, Catherine Prigent, Owen Embury, et al.. Sea Surface Temperature in Global Analyses: Gains from the Copernicus Imaging Microwave Radiometer. Remote Sensing, 2019, 11 (20), pp.2362. 10.3390/rs11202362 . hal-02389453

HAL Id: hal-02389453

<https://hal.science/hal-02389453>

Submitted on 13 Dec 2020

HAL is a multi-disciplinary open access archive for the deposit and dissemination of scientific research documents, whether they are published or not. The documents may come from teaching and research institutions in France or abroad, or from public or private research centers.

L'archive ouverte pluridisciplinaire **HAL**, est destinée au dépôt et à la diffusion de documents scientifiques de niveau recherche, publiés ou non, émanant des établissements d'enseignement et de recherche français ou étrangers, des laboratoires publics ou privés.

1 Article

2 Sea surface temperature in global analyses: gains 3 from the Copernicus Imaging Microwave Radiometer

4 Kevin Pearson ^{1,*}, Simon Good ², Christopher Merchant ¹, Catherine Prigent ³, Owen Embury ¹
5 and Craig Donlon ⁴

6 ¹ Department of Meteorology, University of Reading, PO Box 243, Reading, RG6 6BB, UK

7 ² Met Office, FitzRoy Road, Exeter, EX1 3PB, UK

8 ³ LERMA, Observatoire de Paris, 61 Av. de l'Observatoire, F-75 014 Paris, France

9 ⁴ European Space Agency, ESTEC, Katwijk, Netherlands

10 * Correspondence: k.j.pearson@reading.ac.uk

11 Received: date; Accepted: date; Published: date

12 **Abstract:** Sea surface temperatures (SSTs) derived from passive microwave (PMW) observations
13 benefit global ocean and SST analyses because of their near-all-weather availability. Present PMW
14 SSTs have real aperture-limited spatial resolution in excess of 50 km, limiting the spatial fidelity
15 with which SST features, reflecting ocean dynamics, can be captured. This contrasts with the target
16 resolution of global analyses of 5 to 10 km. The Copernicus Imaging Microwave Radiometer (CIMR)
17 is a mission concept under consideration as a high-priority candidate mission for expansion of the
18 Copernicus space programme. This instrument would be capable of real aperture resolution <15 km
19 with low total uncertainties in the range 0.4–0.8K for channels between 1.4 and 36.5 GHz and a dual-
20 view arrangement that further reduces noise. This paper provides a comparative study of SST
21 uncertainty and feature resolution with and without the availability of CIMR in the future SST-
22 observing satellite constellation, based on a detailed simulation of CIMR plus infra-red observations
23 and the processing of global SST analyses with 0.05° final grid resolution. Simulations of CIMR data
24 including structured errors were added to an observing system consisting of the Sea and Land
25 Surface Radiometer (SLSTR) on Sentinel-3A and the Advanced Very High Resolution Radiometer
26 (AVHRR) on MetOp-A. This resulted in a large improvement in the global RMSE for SST from 0.37K
27 to 0.21K for January and 0.34K to 0.23K for July. There was a particularly noticeable improvement
28 in the performance of the analysis, as measured by the reduction in RMSE, for dynamical and
29 persistently cloudy areas. Of these, the Aghulas current showed an improvement of 43% in January
30 and 48% in July, the Gulf Stream 70% and 44%, and the Maritime Continent 50% and 40%.

31 **Keywords:** passive microwave; sea surface temperature; CIMR; OSTIA;

32

33 1. Introduction

34 Measurement of sea surface temperature (SST) is crucial to the understanding and prediction of
35 the atmosphere and ocean. SST regulates the exchange of moisture and heat [1,2] between the two
36 and thus controls the thermal structure of the upper ocean and sets the boundary conditions needed
37 for numerical weather prediction. Errors in SST can lead directly to a decrease in NWP skill [3]. SSTs
38 retrieved from infrared (IR) sensor data generally have superior spatial resolution (~1 km) and
39 retrieval accuracy (0.2 to 0.4 K) to passive microwave (PMW) sensors (~50 km and 0.35 to 0.5 K for
40 recent and current missions) [4–7]. However, they are limited to cloud-free regions whereas PMW
41 sensors are able to make measurements through cloud. This greatly increases their coverage and
42 makes them particularly important for regions of persistent cloud such as the high-latitudes in winter.

43 The Copernicus Imaging Microwave Radiometer (CIMR) is a mission concept under
 44 consideration as a high-priority candidate mission for expansion of the Copernicus space programme
 45 (the Sentinels). The concept includes deployment of a ~7 m mesh antenna capable of real aperture
 46 resolution <15 km at 6.9 GHz (required for cool-water SST estimation). The CIMR mission is
 47 motivated by the EU Arctic policy [8], whereby monitoring of the physical properties of the changing
 48 high-latitude environment is essential for sustainability, economic development and environmental
 49 protection. Its primary objectives are the retrieval of sea ice concentration (SIC) and SST. The
 50 requirement for SIC is for spatial resolution ≤ 5 km with a total standard uncertainty of $\leq 5\%$ and for
 51 SST is spatial resolution ≤ 15 km with a total standard uncertainty of $\leq 0.2 \pm 0.1$ K[9]. The CIMR mission
 52 will deliver both high-latitude and global data with near-global coverage every day. CIMR SSTs will
 53 therefore improve the observability of ocean dynamics reflected in SST compared to an infra-red-
 54 only SST dataset, particularly in areas of persistent cloud: the Arctic, Southern Ocean, north Pacific
 55 and Atlantic oceans, marine stratiform regions, and the inter-tropical convergence zone including the
 56 tropical warm pool. The targets for the uncertainty components are given in Table 1. Measurements
 57 from both the forward and rearward arcs of CIMR's conical scan will be available, enabling averaging
 58 of retrievals to reduce noise. This combination of features implies that CIMR SSTs are expected to
 59 have simultaneously higher spatial resolution and lower noise uncertainty than present PMW SSTs
 60 [9].

61 Table 1 Uncertainty components for each of the CIMR channels. The columns give the total
 62 uncertainty as well as the radiometric, orbital stability, lifetime-stability and pre-launch calibration
 63 contributions to the total uncertainty budget.

Channel (GHz)	U_{total}	$U_{NE\Delta T}$	$U_{orb-stab}$	$U_{life-stab}$	U_{pl-cal}
1.41	0.5	0.3	0.2	0.2	0.2
6.9	0.4	0.2	0.1	0.2	0.2
10.65	0.45	0.3	0.1	0.2	0.2
18.7	0.6	0.4	0.2	0.2	0.2
36.5	0.8	0.7	0.2	0.2	0.2

64
 65 The aim of this study is to examine the effect on SST analyses of adding CIMR to the IR-observing
 66 constellation, here represented by the Advanced very-high-resolution radiometer (AVHRR)
 67 instrument on-board Met-Op A and by the Sea and Land Surface Temperature Radiometer (SLSTR)
 68 carried by Sentinel-3A. Synthesised observations were provided as input to the Operational Sea
 69 Surface Temperature and Sea Ice Analysis system (OSTIA) [10] in different combinations as set out
 70 below.

71 The OSTIA system is in operational near-real time use by the Met Office. It operates by ingesting
 72 satellite and in situ SSTs and optimally combining them to produce estimates of daily, global,
 73 foundation SST (defined as SST free of diurnal variability[11,12]). A climate configuration of the
 74 system generates SST analyses from satellite data only, which are representative of the daily average
 75 at 20 cm depth [7] and this is used in this study. For each day, the system generates a background
 76 field based on the persistence of the previous day's analysis, with a weak relaxation to climatology.
 77 For the open ocean, the relaxation timescale is 30 days. The background is combined with the satellite
 78 SSTs with relative weights determined by their uncertainties. A background error covariance matrix
 79 is specified *a priori* based on two components, one representing errors due to mesoscale ocean features
 80 and one capturing larger scale errors such a synoptic weather systems. The uncertainty associated
 81 with each retrieved SST is used with errors assumed to be uncorrelated. The new analysis is then
 82 calculated using the NEMOVAR system[13] to minimize the cost function

$$83 \quad f = \delta x^T \mathbf{B}^{-1} \delta x + \delta y^T \mathbf{R}^{-1} \delta y \quad (1)$$

84 where δx is the difference between the new analysis field and the background state, \mathbf{B} is the
85 background error covariance matrix, δy is the difference between the newly-measured SSTs and
86 those in the background state and \mathbf{R} is the observation error covariance matrix[14].

87 2. Methods

88 To understand the impact of CIMR the future observability of SST, we have undertaken a
89 simulation study that provides synthetic observations to the OSTIA system. By providing input data
90 with and without CIMR observations and with and without realistic observational errors, we can test
91 the effect of the increased coverage provided by adding CIMR data to the IR constellation and
92 whether this effect remains when allowance is made for the increased uncertainties associated with
93 PMW-derived SSTs. To achieve this, a “truth” dataset was required from which simulated
94 observations for CIMR, SLSTR and AVHRR could subsequently be derived and to which analysis
95 fields could be compared. To act as SST truth, we obtained data generated as part of the North
96 Atlantic Climate System Integrated Study (ACSIS) [15], consisting of the output of a free-running
97 coupled general-circulation simulation using the Nucleus for European Modelling of the Ocean
98 (NEMO) model [16]. These data were provided on the tripolar, curvilinear, ORCA12 grid[17,18], with
99 approximate $1/12^\circ$ resolution, and regridded here to an equiangular 0.05° grid for input to OSTIA.
100 As the ORCA grid is slightly coarser than the target OSTIA grid, there is the potential for loss of
101 feature resolution at the smallest scales. Consequently, sharpening was applied, using a 2-D
102 Laplacian filter, to increase the power at shorter length scales to match the $-11/3$ power law expected
103 for sea surface height and SST in the open ocean [19-21].

104 In order to simulate IR observations of the “truth” dataset with appropriate spatial coverage, it
105 was necessary to apply realistic masking to the data. The largest single cause of invalid IR-based SST
106 values over the ocean, within the satellite swath, is the presence of cloud. Suitable masking was
107 achieved using L3U data for the two IR instruments from 2018 generated with the processor (GBCS)
108 used for the Sea Surface Temperature Climate Change Initiative project [7,22-24] and the Copernicus
109 Climate Change Service Climate Data Store [25,26]. L3U data were generated at 0.05 resolution with
110 multiple files a day, each corresponding to an input L1 file. The SST in each L3U file was replaced
111 with the value from the “truth” dataset for that day of the year at all locations with a valid SST value
112 and with a quality level of 4 or higher. In January, this results in $14.0 \pm 0.6\%$ of global ocean cells having
113 at least one AVHRR observation on a given day and $12.4 \pm 0.5\%$ having at least one SLSTR observation.
114 Being based on a free-running model, the choice of year for the “truth” data was arbitrary rather than
115 specifically 2018. Model cells with SST less than -1.7°C were interpreted as the locations of sea ice.
116 The resulting dataset constituted the SSTs that would be derived in the case of a perfect observing
117 and retrieval system for the two infrared instruments, given the cloud distribution of the target days.

118 To provide a more realistic observational dataset, synthetic noise was added to the SST in the
119 “perfect” files based on the uncertainty terms provided for each cell in the L3U files. These are (with
120 typically values for AVHRR) large-scale correlated uncertainty (~ 0.1 K), adjustment uncertainty (0.05-
121 0.1 K), synoptically correlated uncertainty (0.1-1.0 K) and uncorrelated uncertainty (0.05-0.2 K).
122 Large-scale correlated uncertainties are those that arise from effects that can be assumed to be
123 correlated everywhere and over long time scales (such as calibration of the satellite sensor). The
124 adjustment uncertainty arises from the process of adjusting SSTs to a standard time and depth. The
125 synoptically correlated uncertainty arises from correlations in the atmospheric conditions between
126 SST retrievals. Both the adjustment and synoptic uncertainties are assumed to be correlated over 100
127 km for IR sensors and 1 day. Uncorrelated uncertainties arise from effects that are not correlated from
128 location to location such as random noise in the satellite sensors [27,28]. Each of these contributions
129 was considered in turn and, for each, a value was added to the SST in each cell in the perfect dataset
130 of with an appropriate magnitude and correlation properties.

131 A single large-scale noise value was applied to all cells in a given L3U file by selecting a random
132 number from the Gaussian distribution with a standard deviation given by the mean of the large-
133 scale correlated uncertainty values in the corresponding file. Noise values corresponding to the
134 adjustment and synoptically correlated uncertainties were generated using a common method. Here

135 a value was chosen at random for each cell on a 1° resolution grid from a Gaussian distribution with
136 a standard deviation given by the mean of these uncertainties over all of the 0.05° resolution cells
137 falling within the 1° cell. These values were then interpolated back down to 0.05° resolution to give a
138 noise value to add to each cell of an appropriate size, that varied smoothly and had correlations over
139 the correct lengthscale (~100 km) for synoptic weather systems. The uncorrelated uncertainty values
140 for each cell were used directly by choosing a random number chosen from a Gaussian distribution
141 with the given standard deviation.

142 Representative daily L3C CIMR data were also generated based on the model “truth” dataset.
143 An initial sea ice mask was applied on the same basis as for the IR data. The edges of the mask were
144 extended by two additional cells in both latitude and longitude to represent the need to avoid side-
145 lobe contamination when measuring SST. A median filter was subsequently applied over a 3x3 box
146 to obtain a SST value as seen by an instrument with a 15 km footprint. These data were then subset
147 to every third pixel in each direction to ensure the independence of each cell being fed to the OSTIA
148 system and a mask was applied to eliminate cells within 25 km of land. Finally, a mask was applied
149 based on the daily coverage expected for the instrument. Analogously to the IR instruments, the
150 resulting data represents the SSTs that would be derived in the case of a perfect observing and
151 retrieval system for CIMR.

152 To ensure the correct weighting of the CIMR observations by the OSTIA system and in order to
153 generate appropriate synthetic observational noise, values were derived for the same 4 uncertainty
154 terms considered for the IR data. The uncorrelated uncertainties were taken from [29] that looked at
155 the result of the instrumental $\text{Ne}\Delta\text{T}$ on the expected retrieval uncertainty of SST from CIMR. The
156 dependence of this uncertainty on SST was retained but, in the absence of specific meteorological
157 information, it was calculated using fixed values of wind speed (7 m s^{-1}), salinity (35 psu) and total
158 column water vapour (14 kg m^{-2}). A similar analysis to [29] that tested the effect of the orbital
159 instability (rather than radiometric) uncertainty on retrieved SST was used to derive values for the
160 synoptically correlated uncertainty of SST. A value of 0.1 K for the adjustment uncertainty was
161 assumed and the large-scale uncertainty term was set to 0 on the assumption of a well-designed and
162 calibrated retrieval scheme that removed orbit-to-orbit biases. An assumption was made that
163 uncertainties were independent across orbits and thus reduced by $\sqrt{N_{obs}}$ for cells with multiple
164 observations on a given day. Noise values were derived from these terms for each cell using the same
165 prescription as for the IR data with the exception that the synoptically correlated uncertainties were
166 derived using a 10°-resolution grid rather than 1°-resolution grid. This ensured a correlation
167 lengthscale of ~1000 km appropriate to the variability in the orbital stability which was assumed to
168 be the dominant effect for this term. An example global SST and the added noise field for CIMR are
169 shown in **Erreur ! Source du renvoi introuvable.**

170

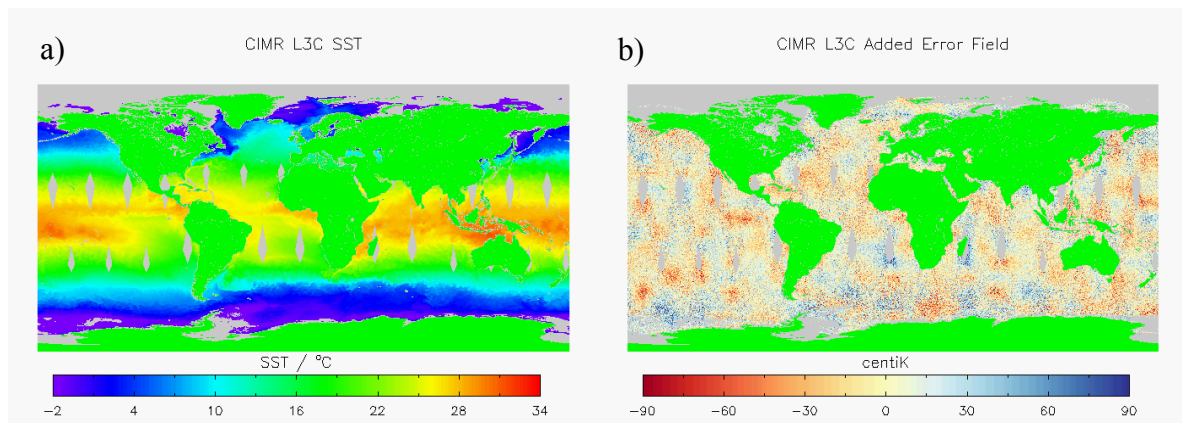


Figure 1 a) Example of the daily SST field from a CIMR L3C file; b) the added error field for this CIMR L3C field

171

172

173

174

175

176

177

178

179

The above datasets were used as input to the OSTIA system in four configurations: “perfect” IR-only, “perfect” combined IR and CIMR, IR-only with realistic errors, and combined IR and CIMR with realistic errors. SST analysis fields were generated for January and July for each configuration. In each case, the first two weeks of the analysis were discarded as a spin-up period and the rest of the month used for assessing the error characteristics of the analysis outputs for each configuration. The data processing methods are summarized in Figure 2 and Figure 3.

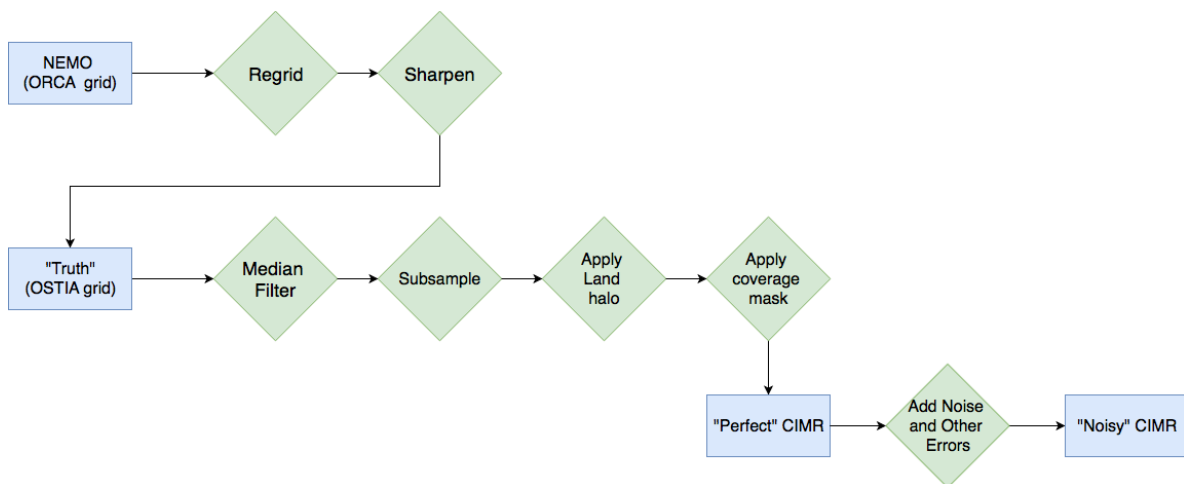


Figure 2 Processing steps involved in generating the synthetic CIMR data

180

181

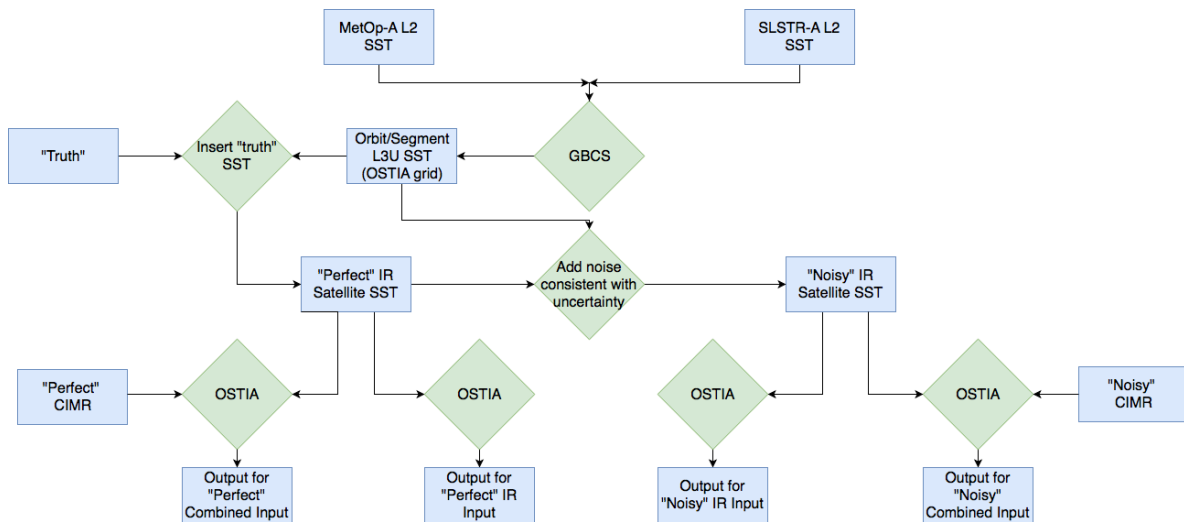


Figure 3 Processing steps involved in creating synthetic SST data for AVHRR and SLSTR

182

183 3. Results

184 3.1. Error Statistics

185 The mean and standard deviation of the error in the daily analysis SST were formed by
 186 comparison with the original “truth” dataset for the day. Histograms of the distribution and global
 187 maps of these statistics are shown for January in Figure 4 and Figure 5 respectively for the perfect
 188 input data cases. Similar comparisons using input data with realistic errors are shown in Figure 6 and
 189 Figure 7. The change in the root-mean-square error (RMSE) resulting from the addition of the CIMR
 190 data to the analysis inputs is shown in Figure 8. Results for July are similar to those for January and
 191 so just the maps of the errors statistics are shown for the data with realistic errors and the change in
 192 RMSE in Figure 9 and Figure 10.

193 Both Figure 4 and Figure 6 show a clear improvement in the error distributions with the addition
 194 of CIMR data and imply an improved ability of the analyses to reproduce the “truth” dataset. As
 195 might be expected, the OSTIA analyses in Figure 5, Figure 7 and Figure 9 show patches of larger error
 196 standard deviations in regions of dynamical SST such as around the Aghulas current and the Gulf
 197 Stream. More widely, for the infrared-only reconstructions, the error standard deviations appear
 198 larger in the southern hemisphere in January and the northern hemisphere in July. This is counter-
 199 intuitive one might expect summer to result in decreased cloudiness and thus improved coverage. In
 200 January, for the southern hemisphere AVHRR and SLSTR have $16.1\pm 0.9\%$ and $14.5\pm 0.9\%$ daily
 201 hemisphere coverage respectively compared to $11.5\pm 0.8\%$ and $10.1\pm 0.5\%$ for the northern
 202 hemisphere. However, in July, there is a more mixed coverage picture: $13.0\pm 1.1\%$ and $12.0\pm 0.8\%$
 203 coverage for the southern hemisphere compared to $10.8\pm 1.1\%$ and $12.5\pm 1.1\%$ for the northern
 204 hemisphere. This implies that rather than coverage, the differences in performance between the
 205 hemispheres is due to increased variability in summer.

206 The differences between northern and southern hemispheres become less pronounced with the
 207 addition of the CIMR data. There are still patches of larger RMSE in the dynamical areas even though
 208 Figure 8 and Figure 10 show that the biggest improvements from the addition of CIMR data are in
 209 these regions. The north-west Pacific in July appears to remain a difficult region to reconstruct. Close
 210 examination shows that the coastal areas have larger RMSE than the open ocean in all the analyses.

211

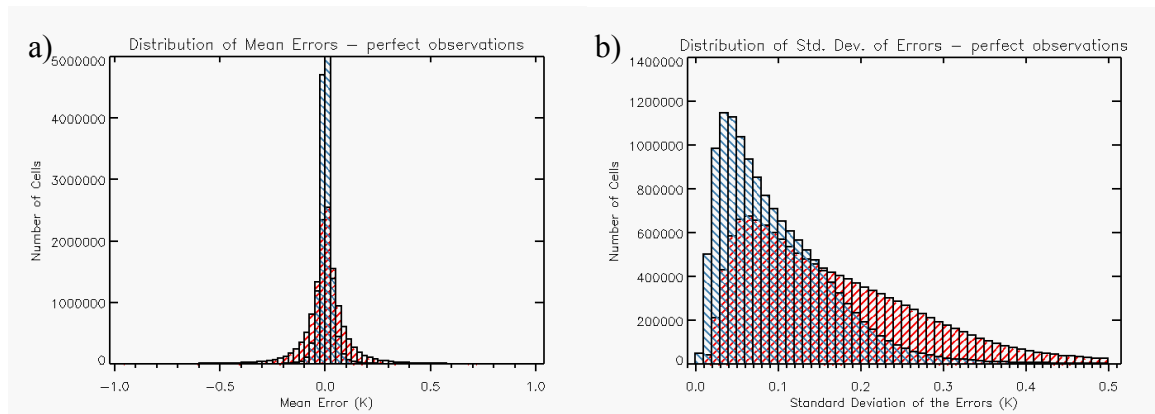


Figure 4 Statistics of the differences between January analysis SST fields and original “truth” SST IR-only (red) and combined IR and MW (blue) input data: (a) Mean error for perfect input; (b) Standard deviation of the error for perfect input.

212

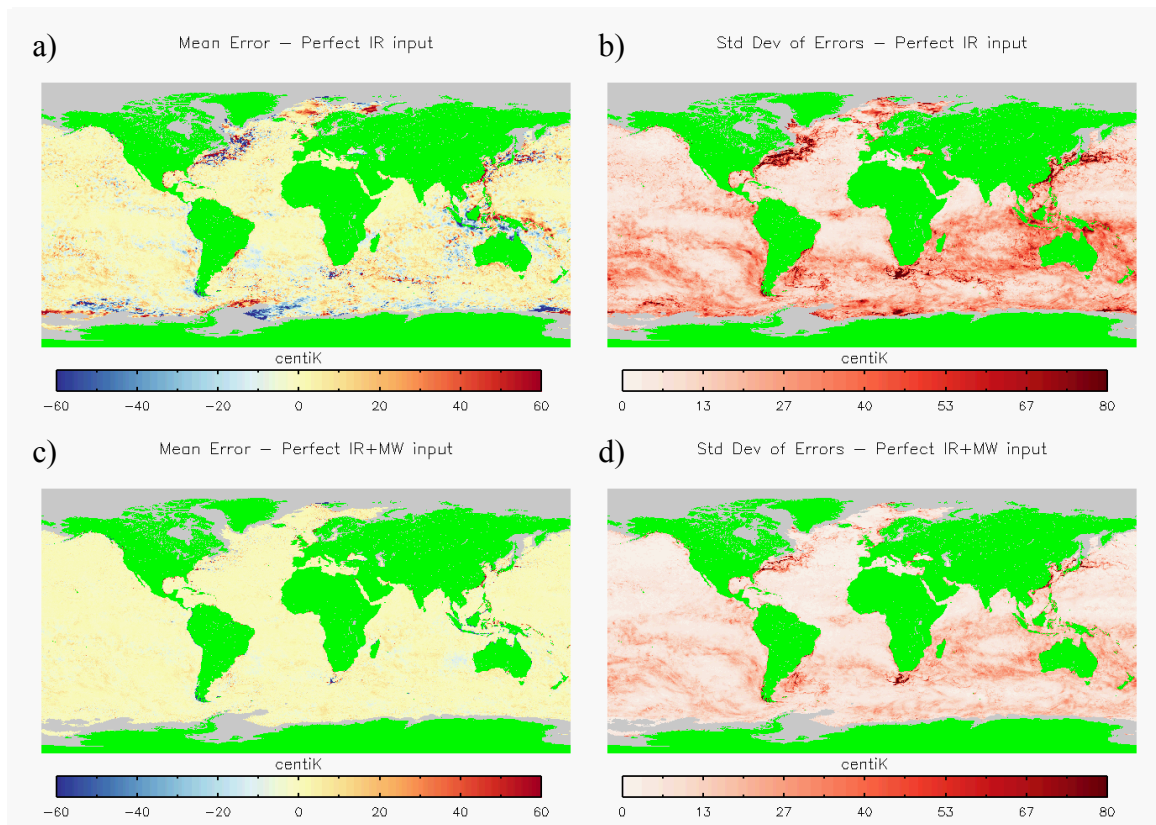


Figure 5 Maps of the January error statistics: a) Mean Error - perfect IR data only; b) Standard deviation of the error - perfect IR data only; c) Mean error - combined perfect IR and CIMR data; d) Standard deviation of the error - combined perfect IR and CIMR data.

213

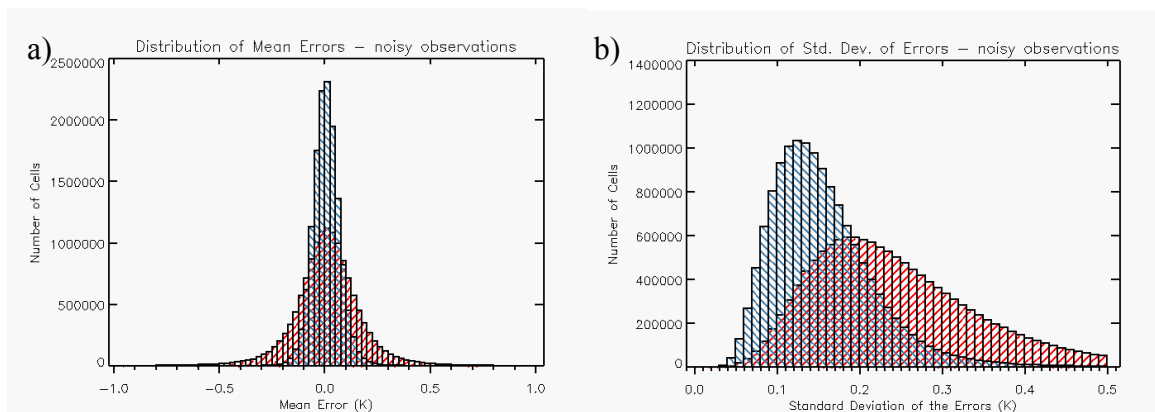


Figure 6 Statistics of the differences between January analysis SST fields and original “truth” SST for IR-only (red) and combined IR and MW (blue) input data with realistic errors: (a) Mean error (b) Standard deviation of the error.

214

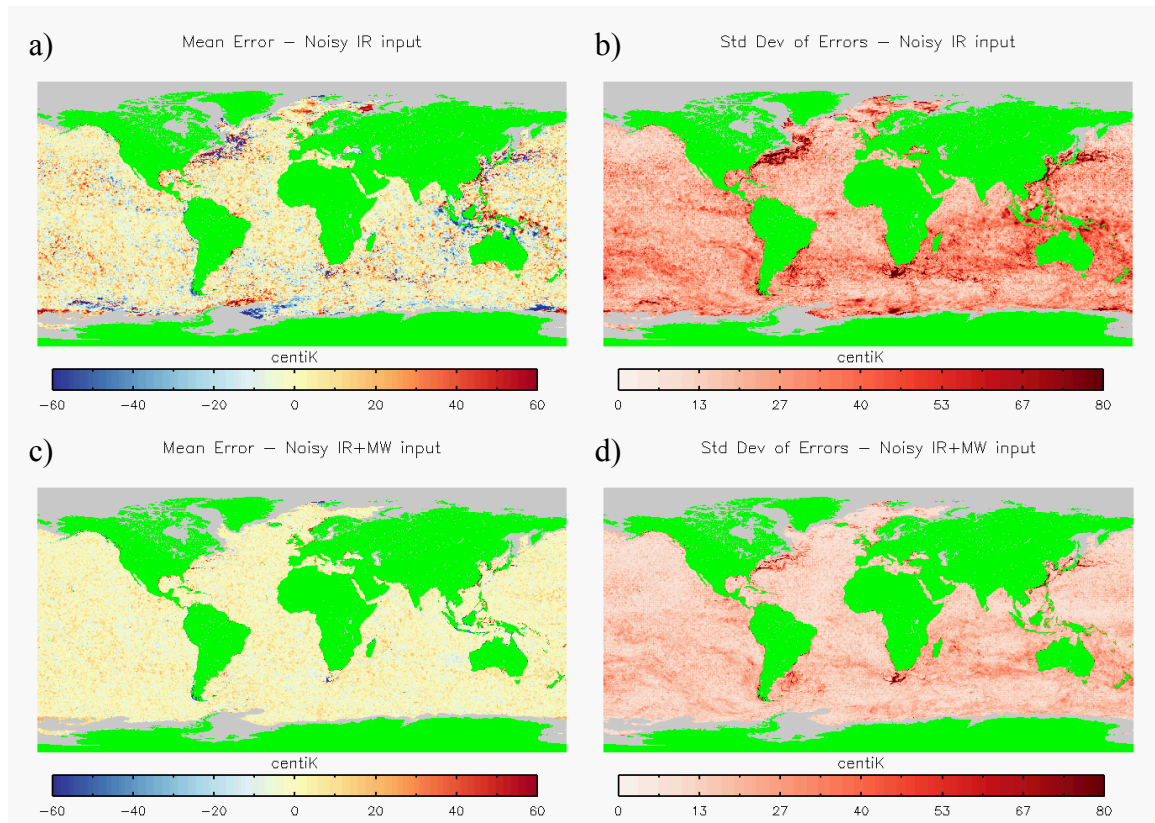


Figure 7 Maps of the error statistics during January for input data with realistic errors: a) Mean Error - IR data only; b) Standard deviation of the error - IR data only; c) Mean error - combined IR and CIMR data; d) Standard deviation of the error - combined IR and CIMR data.

215
216

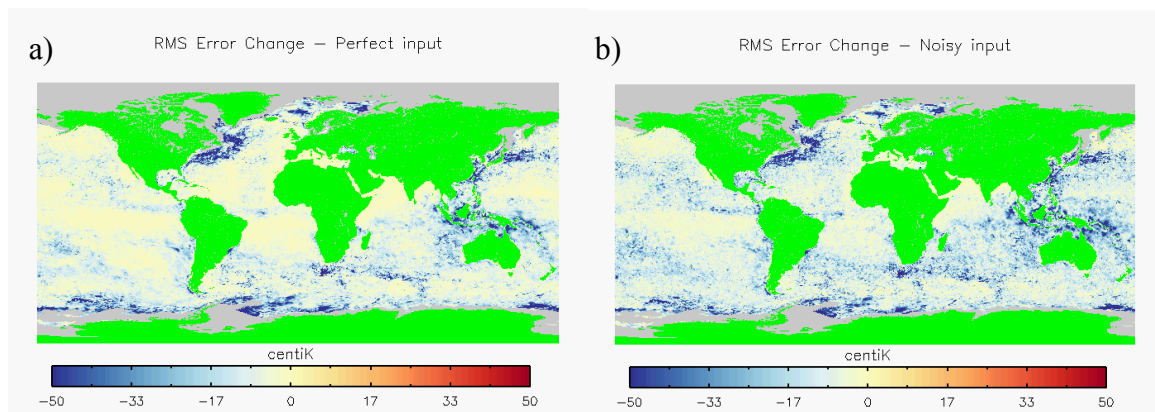


Figure 8 Change in the RMS error of the reconstructed SST field in January from adding CIMR data to the input for: (a) perfect input data; (b) input data containing realistic errors.

217

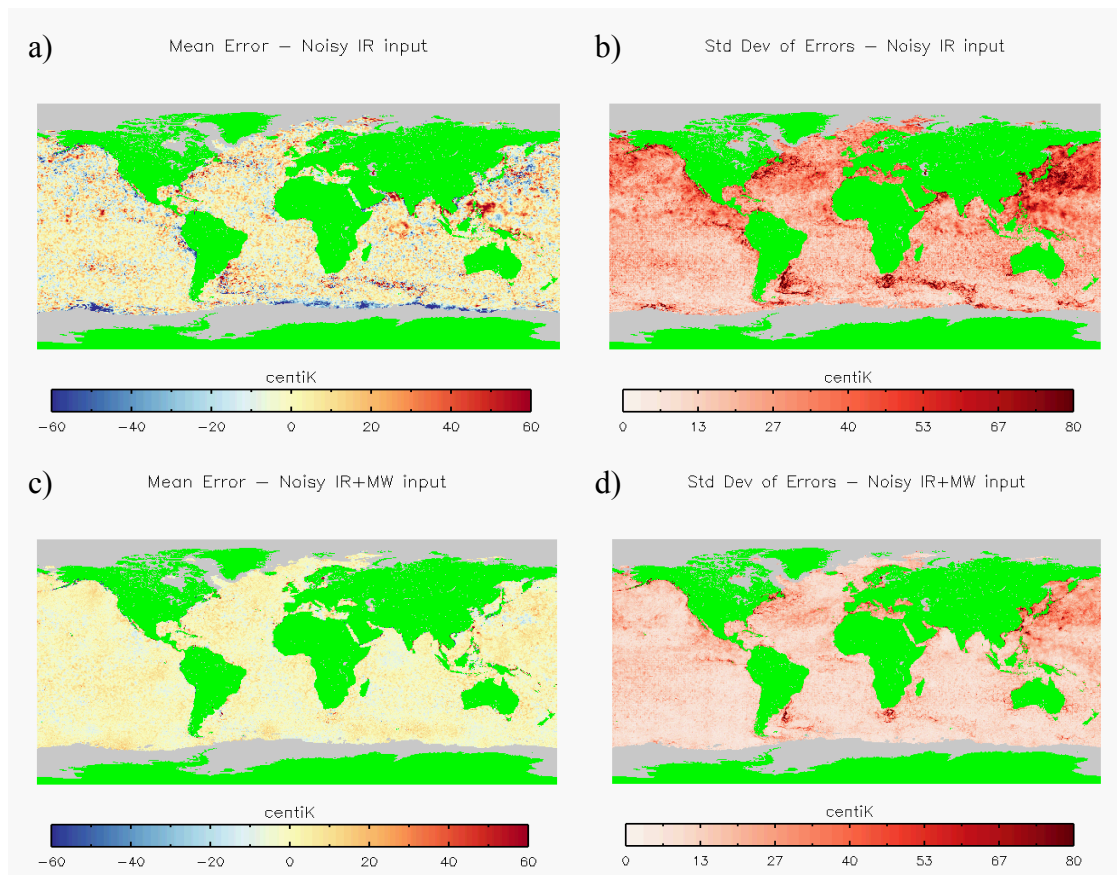


Figure 9 Maps of the error statistics during July for input data with realist errors: a) Mean Error - IR data only; b) Standard deviation of the error - IR data only; c) Mean error - combined IR and CIMR data; d) Standard deviation of the error - combined IR and CIMR data.

218

219

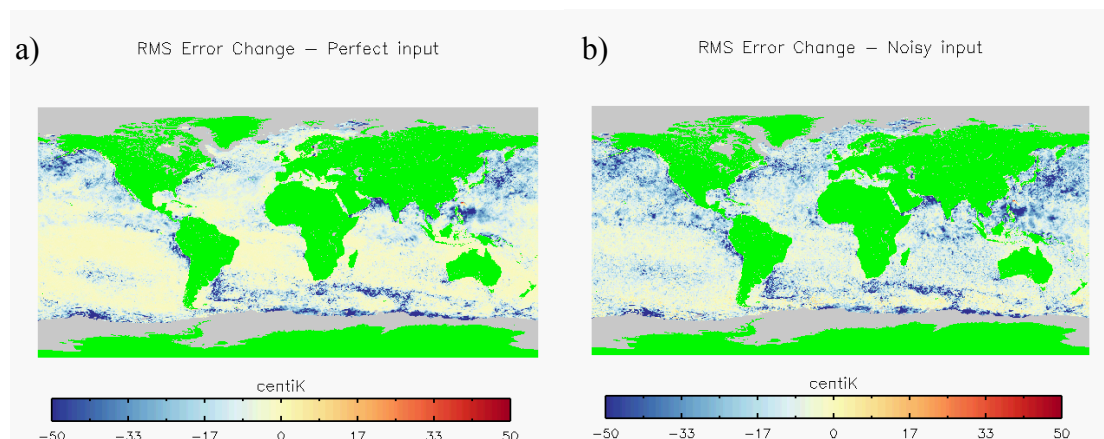


Figure 10 Change in the RMS error of the reconstructed SST field in July from adding CIMR data to the input for: (a) perfect input data; (b) input data containing realistic errors.

220

221

222

A summary of the RMSE in different regions for each of the configurations is given in Table 2. In validation of current operational OSTIA products, RMSE typically ranges 0.3-0.5[14], so the similar

223 magnitude of results in this table suggest that this simulation study is performing realistically. The
 224 addition of CIMR data results in a marked decrease in RMSE in all regions except the coast. The
 225 coastal region (defined as cells less than 25 km from land) shows only small improvements with the
 226 addition of the CIMR data. This is consistent with the restriction of the PMW observations to be
 227 greater than this distance from land. The minimisation step in the NEMOVAR algorithm, however,
 228 is able to spread some information spatially accounting for the small improvement. For the case of
 229 data with realistic errors, the addition of CIMR data results in the global mean RMSE decreasing from
 230 0.369 to 0.210 in January and from 0.338 to 0.225 in July. Improvements of this magnitude in RMSE
 231 suggest CIMR should support a step-change improvement in daily SST analyses.
 232

233 Table 2 Root-mean-square error in different regions for the various experimental configurations

Configuration	Global	Aghulas Current	Gulf Stream	Maritime	Southern Ocean	Coast
Jan						
Perfect IR-only	0.310	0.532	1.286	0.394	0.369	0.641
Perfect IR+CIMR	0.175	0.312	0.358	0.212	0.132	0.608
Realistic IR-only	0.369	0.587	1.289	0.462	0.396	0.667
Realistic IR+CIMR	0.210	0.337	0.386	0.233	0.169	0.622
July						
Perfect IR-only	0.338	0.325	0.410	0.236	0.493	0.981
Perfect IR+CIMR	0.225	0.159	0.258	0.159	0.078	0.969
Realistic IR-only	0.395	0.384	0.506	0.335	0.496	0.995
Realistic IR+CIMR	0.249	0.199	0.284	0.200	0.130	0.969

234
235

236 3.2. Reconstruction in Dynamical regions

237 Figure 11 shows spatial power spectra of the SST fields from the January analysis using the data
 238 with realistic errors for the region of the Aghulas current and Gulf Stream. These are plotted as a ratio
 239 to the “truth” power spectra in these regions and so perfect replication of the truth field in these plots
 240 would give a ratio of 1:1 across the whole spectrum. In both cases there is a marked improvement in

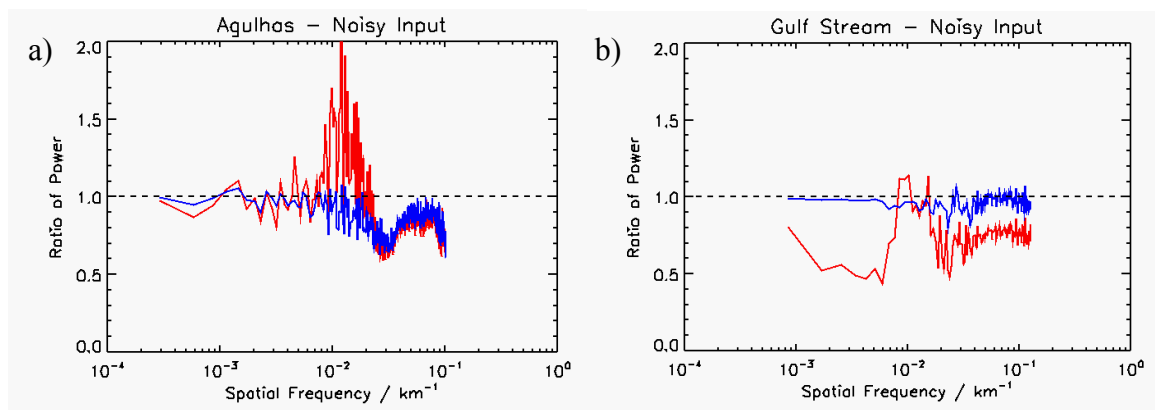


Figure 11 Comparison of the power spectra of the SST field in January from IR-only analysis (red) and combined IR and MW analysis (blue) where both contain realistic input errors. The data are plotted as a ratio to the “truth” SST power spectrum at each wavelength. (a) Aghulas Current region; (b) Gulf Stream region.

241 the agreement with the original “truth” dataset by the addition of CIMR data, as shown by the blue
 242 lines being closer to the 1:1 ratio across almost all spatial frequencies than the red lines.

243 The structure inherent in the SST fields in these regions is shown in Figure 12. This shows a map
 244 of the mean magnitude of the gradient of the SST field in the second-half of January. Figure 13 shows

245 the difference from these fields for the reconstructions using the input data with realistic errors. In
 246 many instances these difference maps show pairs of red and blue areas that would be expected from
 247 a spatial offset of a feature in the SST field. The area of these regions is much reduced by the addition
 248 of CIMR data. The fraction of cells where the magnitude of the difference is greater the $0.02 \text{ } ^\circ\text{C km}^{-1}$
 249 decreases from 6.6 % to 3.1% for the Aghulas Current and from 30.2% to 9.8% for the Gulf Stream. In
 250 some locations there are larger patches of difference eg. just left of centre in Figure 13 (a) and (c) and
 251 bottom left of Figure 13 (b) and (d). Here, in the IR-only case the interpolation scheme has produced
 252 structures not present in the "truth" dataset. These are artefacts resulting from interpolation of data
 253 that are too sparse. This limitation of optimal interpolation in regions with strong SST gradients was
 254 noted in the context of an AVHRR-only reconstruction by [30] and discussed more generally in [31].
 255 With the sparser coverage of the IR-only case, the analysis only has input observations of these
 256 structures intermittently: the analysis gets to "see" the evolving structures on some days and
 257 reconstructs the features only at their locations on those days. The discrete nature of these locations
 258 persists in the time intervals without observations and ultimately becomes apparent in the mean over
 259 the period. The better coverage achieved with CIMR, improves the sampling so that there is a more
 260 representative set of positions for the structures over the period and thus a better representation of
 261 the mean field. These artefactual structures have been greatly reduced with the addition of CIMR
 262 data because the true structures are sampled at a resolution that usefully resolves their locations on
 263 most days.
 264
 265

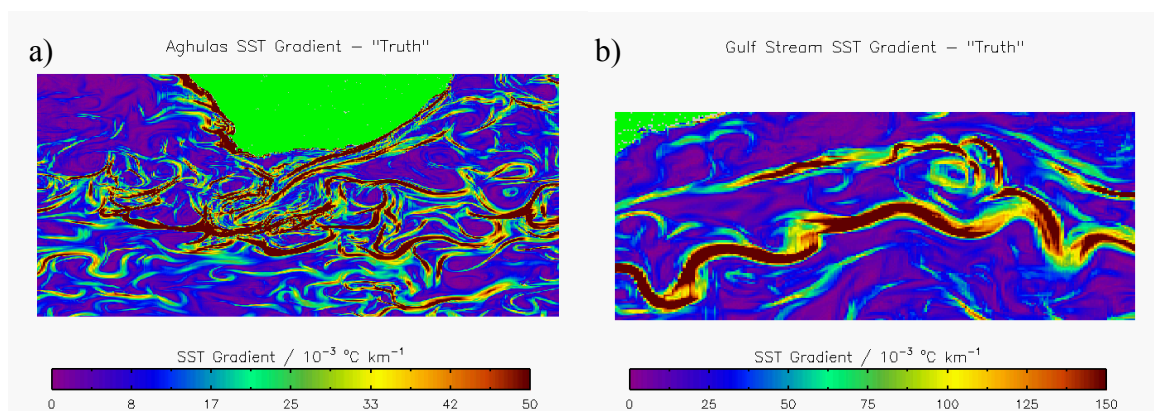


Figure 12 Gradient of the SST field in January in the "truth" data set for: (a) Aghulas Current region; (b) Gulf Stream region.

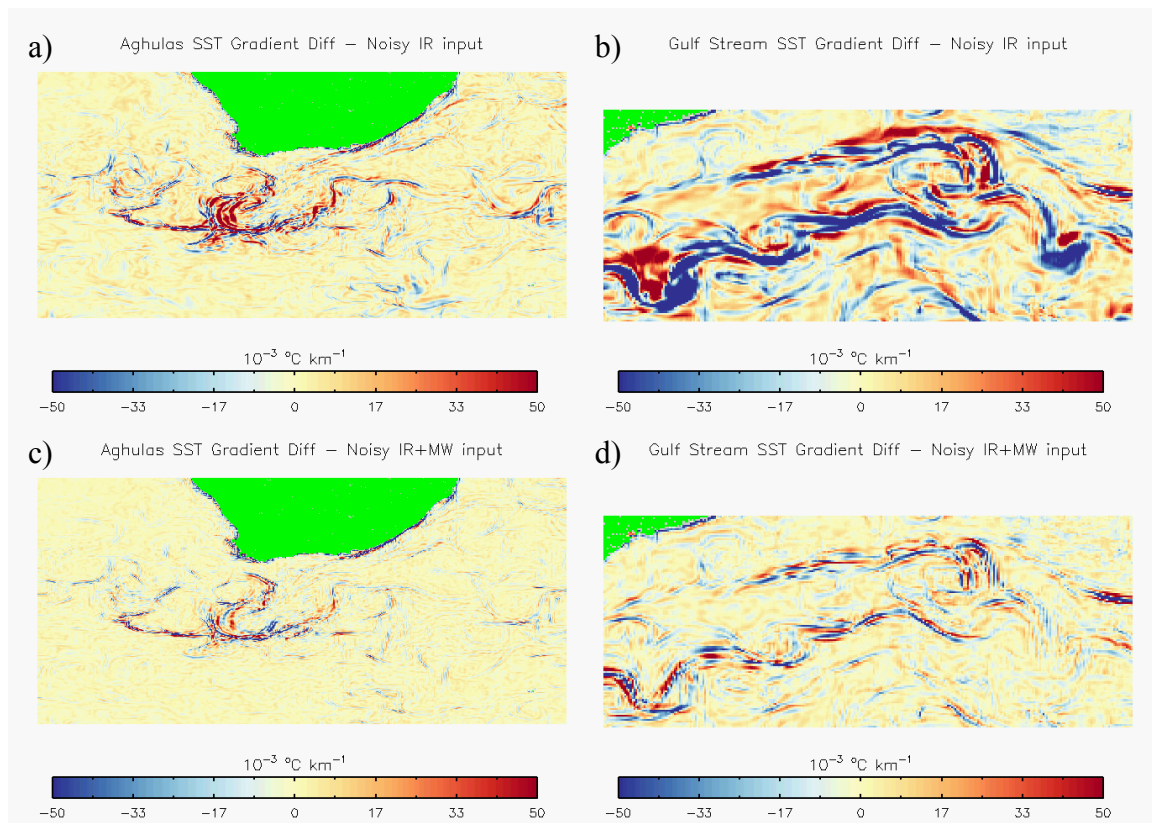


Figure 13 Difference from the “truth” SST gradient field in January for output of OSTIA reconstructions using input data with realistic errors: (a) IR-only data – Aghulas current region; (b) IR-only data- gulf stream region; (c) Combined IR and MW data – Aghulas current region; (d) Combined IR and MW data – Gulf stream region.

267

268 In summary, adding CIMR data to the IR constellation reduces both the mean error and error
 269 standard deviation globally. There is also clear improvement in areas of particular challenge such as
 270 around strong ocean temperature gradients and dynamics and regions of persistent cloud. The
 271 “perfect” data results show that this is a result of the improved coverage available from CIMR despite
 272 the lower weight given to each of the individual observations compared to the IR. The fact that this
 273 improvement remains when data with realistic errors is used show that this improvement will hold
 274 true when CIMR is added to an IR-only constellation in the future.

275 4. Conclusions

276 We have conducted an investigation into the effect of adding CIMR to an IR-only observing system
 277 on global analyses of SST. Adding CIMR resulted in a reduction in the global RMSE of SST in analysis
 278 data from 0.37 K to 0.21 K for January and 0.34 K to 0.23 K for July. There were also strong
 279 improvements in dynamical regions such as the Aghulas current (from 0.59 K to 0.39 K in January and
 280 0.38 K to 0.20 K in July) and Gulf Stream (from 1.29 K to 0.39 K in January and 0.51 K to 0.29 K in
 281 July). There were noticeable examples of artefacts in the reconstruction being removed with the
 282 additional coverage provided by CIMR.

283 CIMR would make an important contribution to global observations of SST and result in a large
 284 reduction in the errors in analyses. Its near-daily coverage and ability to provide SST in the presence
 285 of clouds would significantly improve the analysis reconstruction of dynamical regions where there
 286 are strong SST contrasts and in regions with persistent cloud coverage.

287 **Author Contributions:** Conceptualization, C.M. and C.D.; methodology, K.P. and C.M.; software, K.P., S.G. and
 288 O.E.; validation, K.P.; formal analysis, K.P.; investigation, K.P., O.E. and C.P.; resources, C.M.; data curation,

289 K.P. and O.E.; writing—original draft preparation, K.P.; writing—review and editing, K.P., S.G., C.M., C.D. and
290 C.P.; visualization, K.P.; supervision, C.M.; project administration, K.P., C.M. and C.D.; funding acquisition, C.M

291 **Funding:** “This research was funded by the European Space Agency”

292 **Acknowledgments:** The authors thank Adam Blaker and Andrew Coward of the National Oceanography
293 Centre, Southampton, U.K. for access to the model simulations used in this study.

294 **Conflicts of Interest:** The authors declare no conflict of interest. The funders commissioned the study and
295 commented on interim results and this manuscript.

296 References

- 297 1. Clayson, C.A.; Chen, A.D. Sensitivity of a coupled single-column model in the tropics to treatment of
298 the interfacial parameterizations. *Journal of Climate* **2002**, *15*, 1805-1831, doi:10.1175/1520-
299 0442(2002)015<1805:Soacsc>2.0.Co;2.
- 300 2. Webster, P.J.; Clayson, C.A.; Curry, J.A. Clouds, Radiation, and the Diurnal Cycle of Sea Surface
301 Temperature in the Tropical Western Pacific. *Journal of Climate* **1996**, *9*, 1712-1730, doi:10.1175/1520-
302 0442(1996)009<1712:Cratdc>2.0.Co;2.
- 303 3. Chelton, D.B. The Impact of SST Specification on ECMWF Surface Wind Stress Fields in the Eastern
304 Tropical Pacific. *Journal of Climate* **2005**, *18*, 530-550, doi:10.1175/jcli-3275.1.
- 305 4. Donlon, C.; Robinson, I.; Casey, K.S.; Vazquez-Cuervo, J.; Armstrong, E.; Arino, O.; Gentemann, C.;
306 May, D.; LeBorgne, P.; Piollé, J., et al. The Global Ocean Data Assimilation Experiment High-resolution
307 Sea Surface Temperature Pilot Project. *Bulletin of the American Meteorological Society* **2007**, *88*, 1197-1214,
308 doi:10.1175/bams-88-8-1197.
- 309 5. Nielsen-Englyst, P.; L. Høyer, J.; Toudal Pedersen, L.; L. Gentemann, C.; Alerskans, E.; Block, T.;
310 Donlon, C. Optimal Estimation of Sea Surface Temperature from AMSR-E. *Remote Sensing* **2018**, *10*,
311 doi:10.3390/rs10020229.
- 312 6. Pearson, K.; Gentemann, C.; Kachi, M. *Comparison of AMSR2 Sea Surface Temperature Retrievals with in-*
313 *situ data*; Group for High Resolution Sea Surface Temperature: ESA/ESTEC, Noordwijk, Netherlands,
314 2015; pp 74-80.
- 315 7. Merchant, C.J.; Embury, O.; Bulgin, C.E.; Block, T.; Corlett, G.; Fiedler, E.; Good, S.A.; Mittaz, J.; Rayner,
316 N.; Berry, N.A., et al. Satellite-based time-series of sea-surface temperature since 1981 for climate
317 applications. *Scientific Data* **2019**.
- 318 8. EU Arctic Policy. Available online: https://eeas.europa.eu/arctic-policy/eu-arctic-policy_en (accessed on
319 11 June 2019).
- 320 9. Donlon, C. *Copernicus Imaging Microwave Radiometer (CIMR) - Mission Requirements Document*; ESA-
321 EOPSM-CIMR-MRD-3236; European Space Agency: 5 March 2019, 2019.
- 322 10. Donlon, C.J.; Martin, M.; Stark, J.; Roberts-Jones, J.; Fiedler, E.; Wimmer, W. The Operational Sea Surface
323 Temperature and Sea Ice Analysis (OSTIA) system. *Remote Sensing of Environment* **2012**, *116*, 140-158,
324 doi:10.1016/j.rse.2010.10.017.
- 325 11. Donlon, C. *Proceedings from the Third GODAE High Resolution SST Pilot Project Workshop*; 16;
326 International GHRSSST-PP Project Office: Met Office, Fitzroy Road, Exeter, EX3 1PB, United Kingdom,
327 2003.
- 328 12. Donlon, C.; Emery, B.; Kawamura, H.; Cummings, J.; Robinson, I.; LeBorgne, P.; May, D.; Minnett, P.;
329 Barton, I.; Rayner, N., et al. *The Recommended GHRSSST-PP Data Processing Specification GDS*; 17;
330 International GHRSSST-PP Project Office: Met Office, Fitzroy Road Exeter, EX3 1PB, United Kingdom,
331 26 March 2004, 2004.

- 332 13. Mogensen, K.S.; Balmaseda, M.A.; Weaver, A. *The NEMOVAR ocean data assimilation system as*
333 *implemented in the ECMWF ocean analysis for System 4*; Technical Note 668; European Centre for Medium
334 Range Weather Forecasts: 2012.
- 335 14. Fiedler, E.K.; McLaren, A.; Banzon, V.; Brasnett, B.; Ishizaki, S.; Kennedy, J.; Rayner, N.; Roberts-Jones,
336 J.; Corlett, G.; Merchant, C.J., et al. Intercomparison of long-term sea surface temperature analyses using
337 the GHRSSST Multi-Product Ensemble (GMPE) system. *Remote Sensing of Environment* **2019**, *222*, 18-33,
338 doi:10.1016/j.rse.2018.12.015.
- 339 15. The North Atlantic Climate System Integrated Study. Available online: <http://acsis.ac.uk> (accessed on
340 11 June 2019).
- 341 16. Gurvan, M.; Romain, B.-B.; Bouttier, P.-A.; Bricaud, C.; Bruciaferri, D.; Calvert, D.; Chanut, J.; Clementi,
342 E.; Coward, A.; Delrosso, D., et al. NEMO Ocean Model. 2017; <http://doi.org/10.5281/zenodo.1472492>.
- 343 17. Madec, G.; Imbard, M. A global ocean mesh to overcome the North Pole singularity. *Climate Dynamics*
344 **1996**, *12*, 381-388, doi:10.1007/bf00211684.
- 345 18. ORCA tripolar grid. Available online: <https://www.nemo-ocean.eu/doc/node108.html> (accessed on 4
346 July 2019).
- 347 19. Le Traon, P.Y.; Klein, P.; Hua, B.L.; Dibarboure, G. Do Altimeter Wavenumber Spectra Agree with the
348 Interior or Surface Quasigeostrophic Theory? *Journal of Physical Oceanography* **2008**, *38*, 1137-1142,
349 doi:10.1175/2007jpo3806.1.
- 350 20. Isern-Fontanet, J.; Chapron, B.; Lapeyre, G.; Klein, P. Potential use of microwave sea surface
351 temperatures for the estimation of ocean currents. *Geophysical Research Letters* **2006**, *33*,
352 doi:10.1029/2006gl027801.
- 353 21. Fiedler, E.K.; Mao, C.; Good, S.A.; Water, J.; Martin, M.J. Improvements to feature resolution in the
354 OSTIA sea surface temperature analysis using the NEMOVAR assimilation scheme. *Quarterly Journal*
355 *of the Royal Meteorological Society* **2019**.
- 356 22. Mackie, S.; Embury, O.; Old, C.; Merchant, C.J.; Francis, P. Generalized Bayesian cloud detection for
357 satellite imagery. Part 1: Technique and validation for night-time imagery over land and sea.
358 *International Journal of Remote Sensing* **2010**, *31*, 2573-2594, doi:10.1080/01431160903051703.
- 359 23. Mackie, S.; Merchant, C.J.; Embury, O.; Francis, P. Generalized Bayesian cloud detection for satellite
360 imagery. Part 2: Technique and validation for daytime imagery. *International Journal of Remote Sensing*
361 **2010**, *31*, 2595-2621, doi:10.1080/01431160903051711.
- 362 24. Merchant, C.J.; Embury, O.; Roberts-Jones, J.; Fiedler, E.; Bulgin, C.E.; Corlett, G.K.; Good, S.; McLaren,
363 A.; Rayner, N.; Morak-Bozzo, S., et al. Sea surface temperature datasets for climate applications from
364 Phase 1 of the European Space Agency Climate Change Initiative (SST CCI). *Geoscience Data Journal*
365 **2014**, *1*, 179-191, doi:10.1002/gdj3.20.
- 366 25. Copernicus Climate Change Service Dataset: Sea Surface Temperature Integrated Climate Data Record
367 (ICDR) from the Advanced Very High Resolution Radiometer (AVHRR), Level 3C (L3C), version 2.0.
368 Copernicus Climate Change Service 2019.
- 369 26. Climate Data Store. Available online: <https://cds.climate.copernicus.eu/#!/home> (accessed on 8 July
370 2019).
- 371 27. Rayner, N.; Good, S.A.; Block, T.; Evadzi, P.; Embury, O. *SST CCI Product User Guide*; Met Office: 2019.
- 372 28. Bulgin, C.E.; Embury, O.; Corlett, G.; Merchant, C.J. Independent uncertainty estimates for coefficient
373 based sea surface temperature retrieval from the Along-Track Scanning Radiometer instruments.
374 *Remote Sensing of Environment* **2016**, *178*, 213-222, doi:10.1016/j.rse.2016.02.022.

- 375 29. Kilic, L.; Prigent, C.; Aires, F.; Boutin, J.; Heygster, G.; Tonboe, R.T.; Roquet, H.; Jimenez, C.; Donlon, C.
376 Expected Performances of the Copernicus Imaging Microwave Radiometer (CIMR) for an All-Weather
377 and High Spatial Resolution Estimation of Ocean and Sea Ice Parameters. *Journal of Geophysical Research:*
378 *Oceans* **2018**, *123*, 7564-7580, doi:10.1029/2018jc014408.
- 379 30. Reynolds, R.W.; Smith, T.M.; Liu, C.; Chelton, D.B.; Casey, K.S.; Schlax, M.G. Daily High-Resolution-
380 Blended Analyses for Sea Surface Temperature. *Journal of Climate* **2007**, *20*, 5473-5496,
381 doi:10.1175/2007jcli1824.1.
- 382 31. Reynolds, R.W.; Chelton, D.B.; Roberts-Jones, J.; Martin, M.J.; Menemenlis, D.; Merchant, C.J. Objective
383 Determination of Feature Resolution in Two Sea Surface Temperature Analyses. *Journal of Climate* **2013**,
384 *26*, 2514-2533, doi:10.1175/jcli-d-12-00787.1.
385
386
387



© 2019 by the authors. Submitted for possible open access publication under the terms and conditions of the Creative Commons Attribution (CC BY) license (<http://creativecommons.org/licenses/by/4.0/>).

388

389